energies

MDPI

Article

Improving the Efficiency of Organic Solar Cells via the Molecular Engineering of Simple Fused Non-Fullerene Acceptors

Elizaveta D. Papkovskaya [1], Ji Wan [2], Dmitry O. Balakirev [1], Ivan V. Dyadishchev [1], Artem V. Bakirov [1,3], Yuriy N. Luponosov [1], Jie Min [2,*] and Sergey A. Ponomarenko [1,*]

[1] Enikolopov Institute of Synthetic Polymeric Materials of the Russian Academy of Sciences, Profsoyuznaya St. 70, Moscow 117393, Russia
[2] The Institute for Advanced Studies, Wuhan University, Wuhan 430072, China
[3] Scientific and Research Centre Kurchatov Institute, 1 Kurchatov Square, Moscow 123182, Russia
* Correspondence: min.jie@whu.edu.cn (J.M.); ponomarenko@ispm.ru (S.A.P.)

Abstract: The development of novel non-fullerene small-molecule acceptors (NFAs) with a simple chemical structure for high-performance organic solar cells (OSCs) remains an urgent research challenge to enable their upscaling and commercialization. In this work, we report on the synthesis and comprehensive investigation of two new acceptor molecules (BTPT-OD and BTPT-4F-OD), which have one of the simplest fused structures among the Y series of NFAs, along with the medium energy bandgap (1.85 eV–1.94 eV) and strong absorption in the visible and near-IR spectral range (700–950 nm). The novel NFAs have high thermal stability, good solubility combined with a high degree of crystallinity, and deep-lying levels of the lowest unoccupied molecular orbital (up to −3.94 eV). The BTPT-OD with indan-1-one-3-dicyanvinyl terminal acceptor group is superior to its counterpart BTPT-4F-OD with 5,6-difluorindan-1-one-3-dicyanvinyl group both in the number of synthetic steps and in the photovoltaic performance in OSCs. PM6:BTPT-OD systems exhibit superior photovoltaic performance due to the higher charge mobility and degree of photoresponsiveness, faster carrier extraction, and longer carrier lifetime. As a result, BTPT-OD has almost two times higher photovoltaic performance with PM6 as a donor material due to the higher J_{SC} and FF than BTPT-4F-OD systems. The results obtained indicate that further development of OSCs can be well achieved through a rational molecular design.

Keywords: synthesis of small molecules; push–pull molecules; organic photovoltaics; thermal properties; crystallinity

Citation: Papkovskaya, E.D.; Wan, J.; Balakirev, D.O.; Dyadishchev, I.V.; Bakirov, A.V.; Luponosov, Y.N.; Min, J.; Ponomarenko, S.A. Improving the Efficiency of Organic Solar Cells via the Molecular Engineering of Simple Fused Non-Fullerene Acceptors. *Energies* **2023**, *16*, 3443. https://doi.org/10.3390/en16083443

Academic Editors: Jürgen Heinz Werner, James M. Gardner and Jeff Kettle

Received: 14 December 2022
Revised: 3 March 2023
Accepted: 11 April 2023
Published: 14 April 2023

1. Introduction

In the past few years, organic solar cells (OSCs) have rapidly achieved a high power conversion efficiency (PCE) of over 19%, mostly due to significant advances in the development of non-fullerene acceptors (NFAs) for the photoactive layer of OSCs and the optimization of bulk heterojunction (BHJ) photovoltaic devices [1–9]. A distinctive feature of OSCs compared to other types of photovoltaic cells such as quantum dot-sensitized solar cells (QDSCs) and perovskite solar cells (PSCs) is the possibility of obtaining flexible, lightweight, semitransparent devices, which allows them to be integrated into buildings, vehicles, textiles, or wearable electronics [10–17]. Additionally, the possibility of manufacturing through modern low-cost and fast printing technologies as well as the expected lifetime of more than 10 years [18–20] make OSCs particularly attractive from an economic point of view [21–23].

The development of electron donor and electron acceptor materials plays a key role in the efficient functioning of organic photovoltaic devices. Compared to fullerene-based acceptor materials, NFAs offer significant advantages. Due to the possibility of a wide variation of structural units in NFA molecules, the properties of such compounds (absorption

spectrum, thermal, structural and charge-transporting properties, morphology, etc.) can be finely tuned for a certain donor material. The discovery of Y-like structures (Y6 and its derivatives) has led to great interest among researchers. Y6-based OSCs exhibited the expanded absorption of light (up to 950 nm) and sufficient drive force to produce a large J_{SC} over 25 mA/cm^2 and characterized by a low energy loss, resulting in an impressive PCE of 15.7% [24–26]. Tens of different Y-like NFAs have been reported [21,27]. This class of NFAs is among the most promising, and a PCE of over 19% has been achieved using them in single-junction OSCs [7,9,25,28]. However, there are still unresolved essential issues, primarily related to the complexity of the synthesis of Y-like NFAs, which hinder their commercialization. Moreover, the structure–property–device performance correlations are not completely understood. Therefore, the search for novel efficient Y-like NFAs with a simple chemical structure and the investigation of their properties are urgent issues.

Earlier attempts have been made to simplify the structures of the Y-series molecules [24,29–32]. The BTPT-4F being one of the simplest Y-like molecules demonstrated a PCE of 1.09% in single-junction OSCs [24]. The authors explained the low PCE mainly by the limited solubility of BTPT-4F and strong aggregation in the photoactive layer. However, it is still confusing how the individual change in the fused-ring skeleton length or side alkyl chains affects the photovoltaic properties of the molecule, especially film morphology and electron mobility.

In this work, we synthesized two novel NFAs with one of the simplest Y-series structures, containing a central fragment based on benzo[c][1,2,5]thiadiazole, thieno [2′,3′:4,5]pyrrol, solubilizing 2-octyldodecyl chains and either indan-1-one-3-dicyanvinyl (**BTPT-OD**) or 5,6-difluoro-indan-1-one-3-dicyanvinyl (**BTPT-4F-OD**) terminal acceptor units (Figure 1). Generally, introducing additional non-covalent interactions such as F···H and F···π interactions diversifies packing patterns. Fluorine-free NFAs show face-to-face and compact packing, while fluorinated NFAs show more complex and compact 3D stacking [33]. One would expect that the molecular packing of fluorinated compounds should be more compact and, therefore, the devices based on them should exhibit high charge mobility and PCE. However, in this work, we observed that the simpler and fluorine-free **BTPT-OD** has higher values of charge mobility and PCE with PM6 as a donor material as compared to its more complicated analog—**BTPT-4F-OD** with the terminal fluorine-containing acceptor groups.

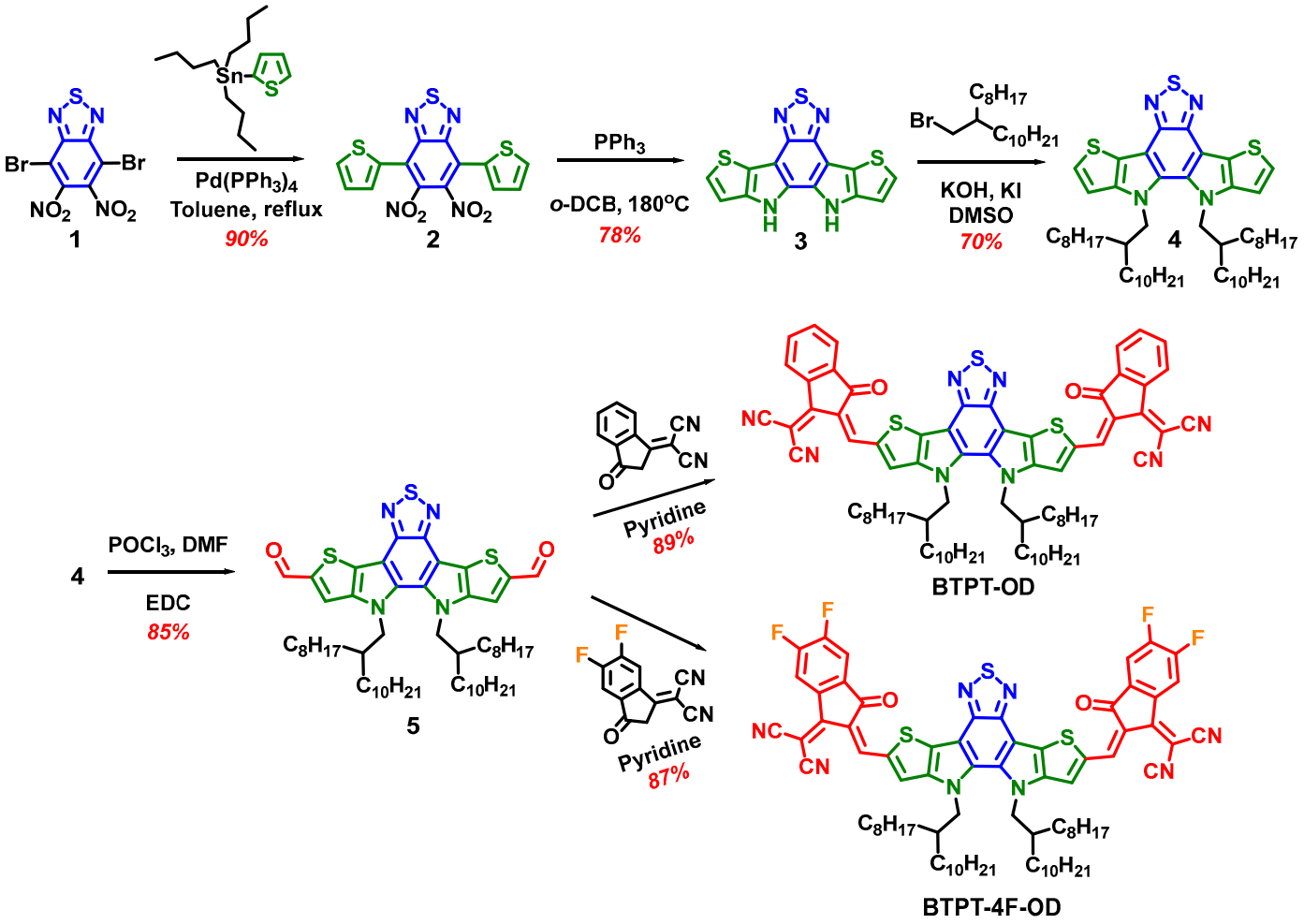

Figure 1. Synthesis of **BTPT-OD** and **BTPT-4F-OD**.

2. Materials and Methods

2.1. Materials

Thiophene, triphenylphosphine, *tetrakis*(triphenylphosphine) palladium (0), tributyltin chloride, 2,1,3-benzothiadiazole, 1,1-dicyanomethylene-3-indanone and n-butyllithium (*n*-BuLi) (2.5 M concentration solution in hexane) were acquired from Sigma-Aldrich Co. and used without further purification. According to the known methods, *o*-dichlorobenzene (*o*-DCB), toluene, dimethylformamide (DMF), dimethyl sulfoxide (DMSO), ethylene dichloride (EDC), and pyridine were purified and dried, and then used as solvents. All reactions, unless stated otherwise, were performed in an inert argon atmosphere using anhydrous solvents. In the case of column chromatography, silica gel 60 (Merck, Darmstadt, Germany) R was taken. PM6 and were purchased from Solarmer Materials Inc., Beijing., China.

4,7-Dibromo-5,6-dinitrobenzo[c][1,2,5]thiadiazole (**1**) [34], 2-(tributylstannyl) thiophene [35], 1-bromo-2-octyldodecane [36], 2-(5,6-difluoro-3-oxo-2,3-dihydro-1H-inden-1-ylidene)malononitrile [37] were obtained as reported elsewhere.

2.2. General Methods

"Bruker WP-250 SY" spectrometer was used for the registering of ^{1}H *NMR spectra* with operation at 250.13 MHz and using the signal of $CDCl_3$ (7.25 ppm) as a reference standard. Solutions of the analyzed molecules (1%) in $CDCl_3$ were used in the case of ^{1}H NMR spectroscopy. ^{13}C *NMR spectra* were recorded using a "Bruker Avance II 300" spectrometer at 75 MHz. The analyzed molecules were taken in the form of 5% solutions

in $CDCl_3$ for ^{13}C NMR spectroscopy. ACD Labs software was used for the subsequent interpretation of the spectra.

Using the Autoflex II Bruker (resolution FWHM 18,000), equipped with a nitrogen laser (work wavelength 337 nm) and time-of-flight mass-detector working in reflections mode *Mass-spectra (MALDI-TOF)* were recorded (the accelerating voltage was 20 kV). The samples were deposited on a polished stainless-steel substrate. The spectrum was registered in the positive ion mode. The registration of the sample took place at different points, and as a consequence, the resulting spectrum was the sum of 300 spectra. The matrices were 2,5-dihydroxybenzoic acid (DHB) (Acros, 99%) and α-cyano-4-hydroxycinnamic acid (HCCA) (Acros, 99%).

UV–Vis absorption spectra were recorded on a Shimadzu UV-2501PC (Kyoto, Japan) spectrophotometer in the standard 10 mm photometric quartz cuvette using $CHCl_3$ solutions with the concentrations of 10^{-5} M. Thin films subject to *UV−vis-NIR* absorption measurement were spin-casted from chloroform solutions with concentration 10 g/L on optically transparent glass. Analysis of light intensity dependent. All measurements were carried out at room temperature.

Cyclic voltammetry measurements were measured using IPC-Pro M potentiostat. Solid compact layers of the samples obtained by electrostatically rubbing the materials onto a glass-carbon electrode were used. Acetonitrile solution using 0.1 M Bu_4NPF_6 as a supporting electrolyte was used for the experiment. The scan rate was 200 mV s^{-1}. Potentials were quantified in relation to the saturated calomel electrode (SCE). Measurements of film CV were performed in a standard three-electrode cell equipped with the working glass-carbon electrode (s = 2 mm^2), the platinum plate as the counter electrode, and the SCE as the reference electrode. The energies of the highest occupied molecular orbital (HOMO) and the lowest unoccupied molecular orbital (LUMO) were estimated using the first standard oxidation (φ_{ox}) and reduction (φ_{red}) potentials derived from CV experiments as E(HOMO) = $-e(\varphi_{ox} + 4.40)$ (eV) and E(LUMO) = $-e(\varphi_{red} + 4.40)$ (eV), where e is the elementary charge [38,39].

Thermogravimetric analysis (TGA) was measured in a dynamic mode in the temperature range of 30–700 °C using an "STA JUPITER 443 F3 NETZSCH" system (Germany). The heating/cooling rate was 10 °C/min. Molecules were investigated in air and argon flow of 200 mL/min.

"Mettler Toledo DSC30" system was used for *Differential scanning calorimetry* (DSC) scans using a heating/cooling rate of 20 °C/min in the temperature range of +20–250 °C and N_2 flow of 50 mL/min for the samples.

The 2D wide-angle (WAXS) analysis of the samples was carried out at the Kurchatov synchrotron (National Research Center Kurchatov Institute) using the BioMUR station. A 1.7 T bending magnet operating at 8 keV (1.445 A) energy, dE/E of 10^{-3} resolution, and 10^9 photon flux was applied as a source of radiation. Dectris Pilatus 1 M detector was used for the registration of diffraction patterns. The beam size at a sample was 0.3 × 0.2 mm^2 with the distance from the sample to the detector was approximately 150 mm. Silver behenate and NaC($Na_2Ca_3Al_2F_{14}$) were taken as calibration standards and the exposure time was 5 min. Fit2D V18.002 Andy Hammersly/ESRF software was used to integrate and process data.

For performance measurements, *the control solar cell devices* were manufactured using a regular structure of glass/ITO/PEDOT:PSS (40 nm)/Active layer (donor: acceptor (D:A = 1:1.2) for bulk heterojunction (BHJ) blend)/PNDIT-F3N(5 nm)/Ag. The ITO glass has a resistance of around 10 ohms and is cleaned by ultrasonication with deionized water, acetone, and isopropyl alcohol for 15 min each in turn. ITO substrates were cleaned in a UV-ozone purification system for 15 min, after drying by blowing with dry nitrogen. Then, the spin-coating method was used to apply a thin layer of PEDOT:PSS (Xi'an Polymer Light Technology Corp 4083) to the pre-cleaned ITO-coated glass at 4500 rpm for 20 s and then dried at 150 °C for 15 min in an air atmosphere. Solutions of PM6:BTPT-4F-OD or PM6:BTPT-OD with a total concentration of 16 mg mL^{-1} in chloroform were used to pre-

pare the photovoltaic layers due to spin-coating method (3500 rpm for 30 s) in a glovebox followed by thermal annealing at 100 °C for 10 min. A PNDIT-F3N layer with a solution concentration of 1 mg/mL was precipitated on top of the active layer at a rate of 4000 rpm for 30 s. Finally, the top silver electrode (100 nm thickness) was thermally evaporated through a mask onto the cathodic buffer layer under a vacuum of ~5×10^{-6} mbar.

The current-voltage characteristics of the solar cells were determined with a Keithley 2400 source meter unit under AM1.5G (100 mW cm^{-2}) irradiation from a solar simulator (Enlitech model SS-F5-3A). Solar simulator illumination intensity was defined at 100 mW cm^{-2} using a monocrystalline silicon reference cell with a KG5 filter. Short-circuit currents under AM1.5G (100 mW cm^{-2}) conditions were evaluated by the spectral response and convolution with the solar spectrum. Part measuring conditions: scanning voltage from 0.0 V to 1.2 V; the step is 0.02 V; the delay time is 1 ms and the scan mode is sweep.

The external quantum efficiency was measured by a Solar Cell Spectral Response Measurement System QE-R3011(Enli Technology Co., Ltd., Kaohsiung, Taiwan).

Atomic force microscopy (AFM) measurements were measured using a Nano Wizard 4 atomic force microscopy (JPK Inc., Berlin, Germany) in Qi mode to investigate the film's surface morphologies.

Transient photocurrent (TPC) measurements: the corresponding solar cells were excited by a laser diode with a wavelength of 405 nm. The transient photocurrent of the short-circuit devices responded to a 200 µs square pulse from the LED without background illumination. The current traces were measured on a Tektronix DPO3034 digital oscilloscope by recording the voltage drop across a 5-ohm sensor resistor in series with the solar cell. The DC voltage was supplied to the solar cell with an MRF544 bipolar junction transistor in a common collector amplifier configuration.

Transient photovoltage (TPV) measurements were made under open-circuit conditions (1 MΩ), when the devices were directly plugged into an oscilloscope. Then white light LED with various light intensities was used for the illumination of the device. A small optical perturbation was applied with a 405 nm laser diode whose light intensity was controlled to create a voltage perturbation of $\Delta V_O < 10$ mV << V_{OC}. The number of charges generated by the pulse was derived by integrating a photocurrent measurement (50 Ω) without bias light.

J-V characteristics: the variation of J_{SC} as a function of light intensity (decrement of change is set (from 100 to 10 through 10, and 8, 5) calibrated with standard silicon) was investigated.

Space-charge-limited-current (SCLC) measurements were performed using single-carrier designed devices. The dark current-voltage characteristics in the space charge limited (SCL) mode were quantified and analyzed according to the reference. The structure of Glass/ITO/ZnO/Active layer/PNDIT-F3N/Ag (100 nm) was used for the electron-only devices and Glass/ITO/PEDOT:PSS/Active layer/MoO_3/Ag (100 nm) structure was used for the hole only devices, where the Ag was vaporized.

2.3. Synthetic Procedures

5,6-dinitro-4,7-di(2-thienyl)-2,1,3-benzothiadiazole (**2**). Under an inert atmosphere 2-(tributylstannyl)thiophene (7.8 g, 20.9 mmol), 4,7-dibromo-5,6-dinitrobenzo[c] [1,2,5]thiadiazole (3.7 g, 9.6 mmol) and $Pd(PPh_3)_4$ (0.45 g, 0.4 mmol) were dissolved in 160 mL of dry toluene and stirred at reflux for 4 h. After completeness of the reaction, the reaction mixture was concentrated under reduced pressure. The crude product was chromatographically purified on a silica gel column eluted with toluene and then recrystallized from petroleum ether to afford a solid. The solid was filtered and dried under a vacuum to obtain compound **2** (3.4 g, yield: 90%) as an orange solid. ^{1}H NMR (250 MHz, $CDCl_3$) δ (ppm) = 7.72 (dd, J_1 = 5.19 Hz, J_2 = 1.22 Hz, 2H), 7.50 (dd, J_1 = 3.66 Hz, J_2 = 1.22 Hz, 2H), 7.21 (dd, J_1 = 4.89 Hz, J_2 = 3.67 Hz, 2H). ^{13}C NMR (75 MHz, $CDCl_3$) δ (ppm) = 152.18, 141.83, 131.44, 130.96, 128.88, 128.00, 121.47. HR-MS (MALDI-TOF) *m/z* calcd. for ($C_{14}H_6N_4O_4S_3$): 389.96. Found [MH^+]: 390.87.

10,11-dihydro[1,2,5]thiadiazolo[3,4-e]thieno[3,2-b]thieno[2′,3′:4,5]pyrrolo[3,2-g]indole (**3**). Compound **2** (2.6 g, 6.9 mmol) and triphenylphosphine (18.6 g, 70.9 mmol) were dissolved in 30 mL of *o*-DCB. The reaction was stirred at 180 °C for 16 h. Then the solvent was removed under a reduced pressure to give the crude compound **5.** The residue was purified by column chromatography on silica gel (2/1, toluene/ethyl acetate) to give a crude product, then, recrystallized from petroleum ether to obtain a red solid **3** (1.73 g, 78% yield). ^{1}H NMR (250 MHz, $CDCl_3$) δ (ppm) = 11.88 (s, 2H), 7.60 (d, J_1 = 5.19 Hz, 2H), 7.41 (d, J_1 = 5.19 Hz, 2H). ^{13}C NMR (75 MHz, $CDCl_3$) δ (ppm) = 146.94, 141.11, 129.52, 126.65, 118.95, 112.95, 106.66. HR-MS (MALDI-TOF) *m/z* calcd. for ($C_{14}H_6N_4S_3$): 325.98. Found: 325.94.

10,11-di(2-octyldodecyl)[1,2,5]thiadiazolo[3,4-e]thieno[3,2-b]thieno[2′,3′:4,5]pyrrolo-[3,2-g]indole (**4**). Compound **3** (1.20 g, 3.7 mmol), 1-bromo-2-octyldodecane (7.85 g, 21.6 mmol), potassium iodide (0.31 g, 1.8 mmol), potassium hydroxide (0.21 g, 3.7 mmol) were dissolved in DMSO (25 mL) and then the mixture was stirred at 80 °C. The completion of the reaction was monitored by TLC. The residue was extracted with ethyl acetate and H_2O. The organic layers were combined and dried over Na_2SO_4, filtered, and purified with column chromatography on silica gel using toluene/petroleum ether (1/10, *v*/*v*) as the eluent to give yellow solid **4** (2.28 g, 70% yield). ^{1}H NMR (400 MHz, $CDCl_3$), δ (ppm) = 7.4 (d, *J* = 5.19 Hz, 2H), 7.13 (d, *J* = 7.19 Hz, 2H), 4.45 (d, *J* = 7.94 Hz, 4H), 2.05–1.91 (overlapping peaks, 2H), 1.31–1.15 (overlapping peaks, 64H), 1.07–0.71 (overlapping peaks, 12H). ^{13}C NMR (75 MHz, $CDCl_3$) δ (ppm) = 147.56, 145.10, 132.78, 126.41, 121.15, 112.00, 110.58, 54.30, 37.88, 31.89, 31.76, 31.35, 30.41, 29.69, 29.59, 29.53, 29.48, 29.36, 29.29, 29.12, 29.06, 25.53, 25.40, 22.68, 22.60, 14.13, 14.10. HR-MS (MALDI-TOF) *m/z* calcd. for ($C_{54}H_{86}N_4S_3$): 886.60. Found: 886.06.

10,11-bis(2-octyldodecyl)-10,11-dihydro-[1,2,5]thiadiazolo[3,4e]thieno[2′,3′:4,5]pyrrolo[3,2-g]thieno[3,2-b]indole-2,8-dicarbaldehyde (**5**). To a 100 mL two-necked flask, DMF (12 mL) was added and cooled to −10 °C, then phosphorus oxychloride (2.6 mL) was added dropwise. After stirring at the same temperature for 1.5 h, compound **4** (1.06 g, 1.47 mmol) in 25 mL 1,2-dichloroethane was added dropwise to the solution before being heated to room temperature and stirred overnight. The reaction mixture was allowed to cool to room temperature and the mixture was poured into water, and then extracted with dichloromethane. After the collected organic layer was washed with water and brine, the crude product was purified using silica gel using ethyl acetate/hexane (1/10, *v/v*) as eluent, yielding an orange solid of compound **5** (1.03 g, 90%). ^{1}H NMR (400 MHz, $CDCl_3$), δ (ppm) = 10.01 (s, 2H), 7.81 (s, 2H), 4.51 (d, *J* = 7.23 Hz, 4H), 2.04–1.93 (overlapping peaks, 2H), 1.30–1.14 (overlapping peaks, 64H), 1.08–0.78 (overlapping peaks, 12H). ^{13}C NMR (75 MHz, $CDCl_3$) δ (ppm) = 183.00, 147.39, 144.73, 144.52, 134.70, 128.38, 119.71, 112.17, 54.59, 38.30, 31.85, 31.74, 30.39, 29.69, 29.59, 29.51, 29.46, 29.34, 29.29, 29.26, 29.11, 29.06, 25.53, 25.51, 22.65, 22.58, 14.12, 14.08. HR-MS (MALDI-TOF) *m/z* calcd. for ($C_{56}H_{86}N_4O_2S_3$): 942.59. Found: 942.98.

2,2′-((2Z,2′Z)-((10,11-bis(2-octyldodecyl)-10,11-dihydro-[1,2,5]thiadiazolo[3,4-e]thieno[2′,3′:4,5]pyrrolo[3,2-g]thieno[3,2-b]indole-2,8-diyl)bis(methanylylidene))bis(3-oxo-2,3-dihydro-1H-indene-2,1-diylidene))dimalononitrile (**BTTP-OD**). Dicarbaldehyde **5** (0.23 g, 0.25 mmol) and 1,1-dicyanomethylene-3-indanone (0.24 g, 1.23 mmol) were placed in a round-bottom flask and dissolved in chloroform (10 mL) under argon atmosphere. Then pyridine (1 mL) was added drop by drop while stirring. The mixture was stirred at 60 °C for 12 h. After cooling to room temperature, the reaction mixture was concentrated under reduced pressure and purified with column chromatography on silica gel using dichloromethane/petroleum ether (1/1, *v*/*v*) as the eluent to give a dark blue solid. The resulting solid was dissolved in a minimal volume of THF, then precipitated with methanol and filtered to yield a pure BTTP-OD (0.29 g, 90% yield). ^{1}H NMR (250 MHz, $CDCl_3$) δ (ppm) = 8.93 (s, 2H), 8.64–8.73 (m, 2H), 7.93–8.02 (m, 4H), 7.73–7.81 (m, 4H), 4.54 (d, *J* = 7.23 Hz, 4H), 2.14–2.02 (overlapping peaks, 2H), 1.25–0.89 (overlapping peaks, 64H), 0.83–0.75 (overlapping peaks, 12H). ^{13}C NMR (75 MHz, $CDCl_3$) δ (ppm) = 187.04, 159.80, 146.89, 145.91, 139.54, 139.48, 137.61, 136.44, 135.34, 135.25, 134.50, 134.04, 125.35, 124.72,

123.35, 122.52, 114.33, 114.26, 114.25, 113.00, 68.66, 54.51, 37.97, 31.45, 31.35, 30.10, 29.37, 29.15, 29.06, 28.98, 28.88, 28.78, 25.40, 22.20, 22.17, 13.68. HR-MS (MALDI-TOF) *m/z* calcd. for ($C_{80}H_{94}N_8O_2S_3$): 1294.67. Found: 1295.13.

2,2′-((2Z,2′Z)-((10,11-bis(2-octyldodecyl)-10,11-dihydro-[1,2,5]thiadiazolo[3,4-e] thieno pyrrolo[3,2-g]thieno[3,2-b]indole-2,8-diyl)bis(methanylylidene))bis(5,6-difluoro-3-oxo-2,3-dihydro-1H-indene-2,1-diylidene))dimalononitrile (**BTTP-4F-OD**). Dicarbaldehyde **5** (0.20 g, 0.21 mmol) and 2-(5,6-difluoro-3-oxo-2,3-dihydro-1H-inden-1-ylidene)malononitrile (0.24 g, 1.06 mmol) were dissolved in chloroform (10 mL) in a round-bottom flask under argon. Then pyridine (1 mL) was added, and the mixture was stirred at 60 °C 12 h. After cooling to room temperature, the reaction mixture was concentrated under reduced pressure. The concentrated mixture was purified with column chromatography on silica gel using dichloromethane/petroleum ether (1/1, *v*/*v*) as the eluent to give a dark blue solid. The resulting solid was dissolved in a minimal volume of THF, then precipitated with methanol and filtered to yield a pure BTTP-4F-OD (0.26 g, 90% yield). ^{1}H NMR (250 MHz, $CDCl_3$) δ (ppm) = 8.87 (s, 2H), 8.70 (s, 2H), 7.88–7.93 (m, 4H), 4.56 (d, *J* = 7.02 Hz, 4H), 2.27–2.01 (overlapping peaks, 2H), 1.26–0.99 (overlapping peaks, 64H), 0.84–0.75 (overlapping peaks, 12H). ^{13}C NMR (75 MHz, $CDCl_3$) δ (ppm) = 185.15, 157.63, 147.26, 146.59, 139.91, 139.56, 139.46, 138.63, 138.39, 136.22, 135.91, 135.86, 126.82, 126.25, 125.10, 121.98, 114.34, 114.25, 113.71, 70.06, 55.14, 38.60, 31.89, 31.80, 30.63, 29.87, 29.59, 29.54, 29.47, 29.32, 29.23, 25.95, 22.65, 22.60, 14.08. HR-MS (MALDI-TOF) *m/z* calcd. for ($C_{80}H_{90}F_4N_8O_2S_3$): 1366.63. Found: 1366.35.

3. Results and Discussion

3.1. Synthesis and Characterization

The synthesis of **BTPT-OD** or **BTPT-4F-OD** consists of five main steps (Figure 1). First, 5,6-dinitro-4,7-di(2-thienyl)-2,1,3-benzothiadiazole (**2**) was prepared through the Stille cross-coupling reaction between tributyl(2-thienyl) stannane and 4,7-dibromo-5,6-dinitro-2,1,3-benzothiazole (**1**) in 90% yield. Second, the double intramolecular Cadogan reductive cyclization of 2 gave rise to 10,11-dihydro[1,2,5]thiadiazolo[3,4-*e*]thieno[3,2-*b*]thieno[2′,3′:4,5]pyrrolo[3,2-*g*]indole (**3**) in 78% yield. The next step involved the preparation of 10,11-di(2-octyldodecyl)[1,2,5]thiadiazolo [3,4-*e*]thieno[3,2-*b*]thieno[2′,3′:4,5]pyrrolo-[3,2-*g*]indole (4) via *N*-alkylation of **3** with 1-bromo-2-octyldodecyl in 70% yield. The Wilsmeyer-Haak formylation of **4** led to 10,11-*bis*(2-octyldodecyl)-10,11-dihydro-[1,2,5]thiadiazolo[3,4-*e*]thieno[2′,3′:4,5] pyrrolo[3,2-g]thieno[3,2-b]indole-2,8-dicarbaldehyde (**5**) in 90% yield. The synthesis of the target **BTPT-OD** and **BTPT-4F-OD** was carried out by Knoevenagel condensation between dicarbaldehyde **5** and indan-1-one-3-dicyanvinyl or 5,6-difluorindan-1-one-3-dicyanvinyl in high yields 89% and 87%, respectively.

The total reaction yields of **BTPT-OD** and **BTPT-4F-OD** were found to be rather high, 37.2% and 36.3%, respectively. However, it is noteworthy that 4 additional steps should be carried out to prepare 5,6-difluorindan-1-one-3-dicyanvinyl [37], which makes the synthesis of **BTPT-4F-OD** more labor-intensive and significantly decreases the total yield.

BTPT-OD and **BTPT-4F-OD** showed good solubility in many organic solvents such as THF, methylene chloride, chloroform, or toluene at room temperature. The detailed synthetic procedures and characterization data for **BTPT-OD** and **BTPT-4F-OD** as well as all precursors can be found in the Electronic Supplementary Information (ESI).

3.2. Optical and Electrochemical Properties

The optical properties of the molecules synthesized were investigated by *UV–vis* absorption spectroscopy in diluted $CHCl_3$ solutions (10^{-6} M) and thin films (Figure 2a and Table 1). The compounds showed rather similar shapes of the absorption spectra: the bands at the high-energy region (300–420 nm) usually ascribed to π–π* transitions and the intensive bands at 620–840 nm usually ascribed to the ICT [40,41] or with a mixed character [42]. **BTPT-4F-OD** has red-shifted absorption spectra as compared to **BTPT-OD** due to a narrower electrochemical bandgap as discussed below. The absorption spectra of

the thin films were significantly shifted to the long-wavelength region and broadened for both compounds in comparison to their spectra in the solutions.

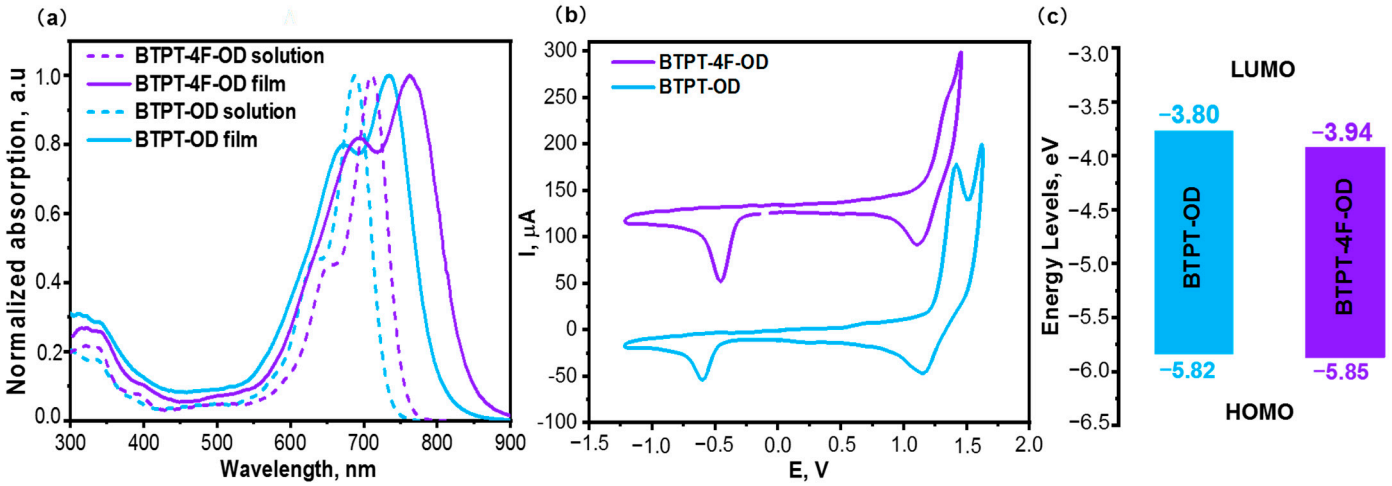

Figure 2. (**a**) *UV–vis* spectra in the chloroform solutions and thin films and; (**b**) CV curves and; (**c**) energy level diagram of the boundary orbitals of **BTPT-OD** and **BTPT-4F-OD**.

Table 1. Optical and electrochemical data of **BTPT-OD** and **BTPT-4F-OD**.

	λ_{max} [a], nm	ε [b] 10^5 (L × mol^{-1} × cm^{-1})	λ_{max} [c], nm	φ_{ox}/HOMO [d], eV	φ_{red}/LUMO [d], eV	E_g [d], eV
BTPT-OD	688	2.10	734	1.42/−5.82	−0.60/−3.80	2.02
BTPT-4F-OD	711	2.05	762	1.45/−5.85	−0.46/−3.94	1.91

[a] λ_{max}—absorption maximum for $CHCl_3$ solutions; [b] molar extinction coefficient in the absorption spectra maximum measured for $CHCl_3$ solutions; [c] λ_{max}—absorption maximum for the thin films; [d] calculated from the CV experiments.

The highest occupied molecular orbital (HOMO) and the lowest unoccupied molecular orbital (LUMO) energies were calculated from the oxidation and reduction potentials measured by cyclic voltammetry (CV) (see Figure 2b,c). The molecules have close HOMO energies (Table 1), since their electron-donating groups are the same. In contrast, the type of terminal electron-withdrawing groups has a pronounced impact on the LUMO energy. The introduction of fluorine atoms into the structure contributed to the shift of reduction potentials to the positive region and thus the LUMO energy was reduced for **BTPT-4F-OD** (−3.94 eV) as compared to its fluorine-free analog—**BTPT-OD** (−3.80 eV). The electrochemical bandgap for **BTPT-OD** and **BTPT-4F-OD** was calculated to be 2.02 eV and 1.91 eV, respectively.

3.3. Thermal and Structural Properties

The thermal and thermo-oxidative stability of **BTPT-OD** and **BTPT-4F-OD** molecules were investigated by thermogravimetric analysis (TGA) and the data are summarized in Figure 3a. The compounds showed high stability both in air and under an argon atmosphere with decomposition temperatures above 320° (calculated for 5% weight loss) without any correlation to the molecular structure.

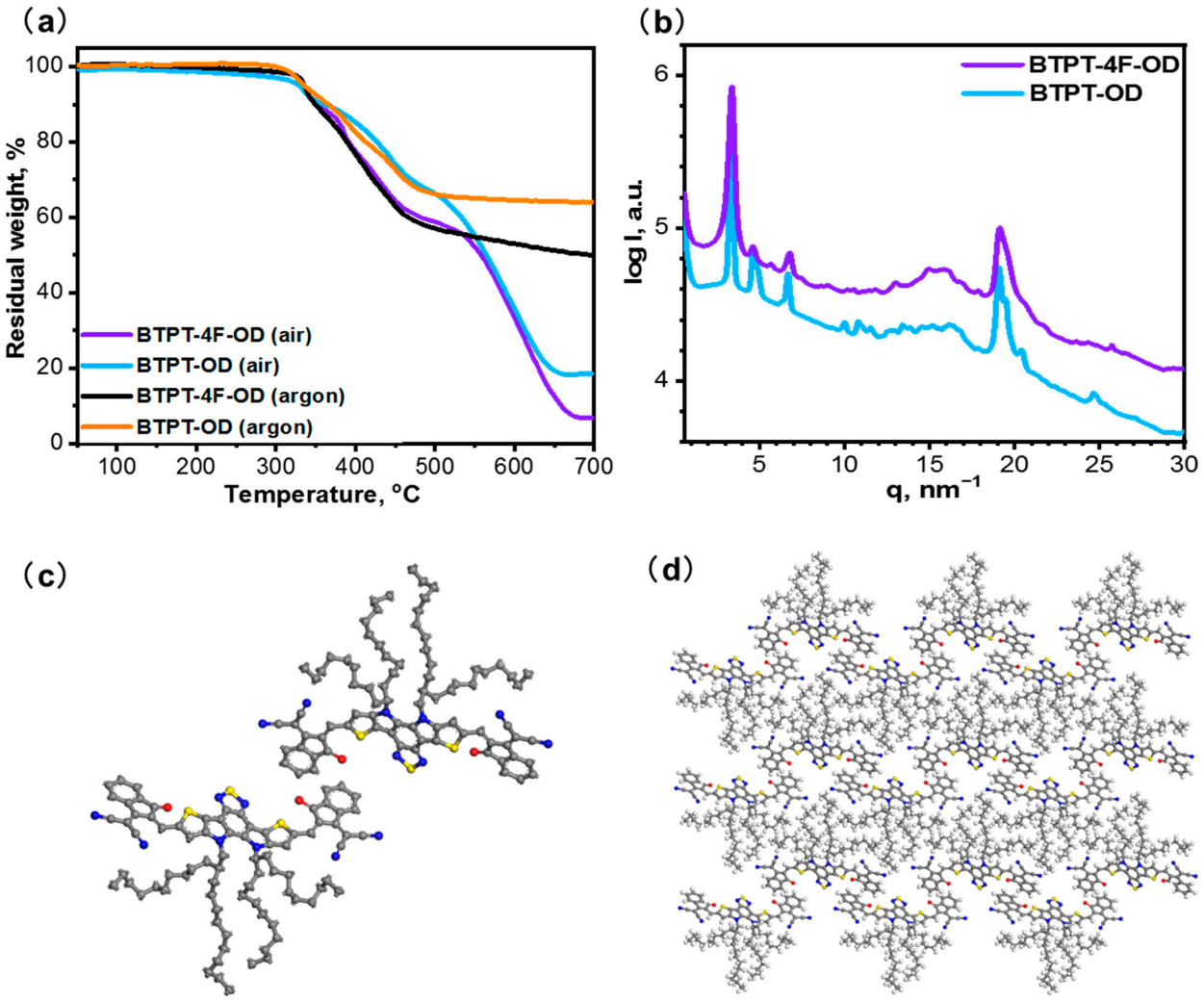

Figure 3. (**a**) Thermogravimetric analysis data in air and in an inert atmosphere and; (**b**) X-ray scattering curves for the **BTPT-OD** and **BTPT-4F-OD** and; (**c**) molecular packing of the **BTPT-OD** molecule into the monoclinic crystal cell X-ray scattering patterns in small and; (**d**) the molecular packing of the **BTPT-OD** to the 3 × 3 crystal lattice; hydrogen atoms were removed for visibility.

The phase behavior of the novel NFAs was investigated by differential scanning calorimetry (DSC). Analysis of the DSC thermograms showed that the DSC method is non-informative for this type of compound, since the phase transitions of the molecules lie at the same temperature region as the thermal destruction processes.

To investigate crystallinity, the 2D wide-angle (WAXS) analysis of the **BTPT-OD** and **BTPT-4F-OD** samples was performed at room temperature, the results of which are shown in Figure 3b. Both samples demonstrated a set of sharp reflections indicating a crystallinity degree of around 50%. The peaks themselves are much narrower for the **BTPT-OD** sample, which leads to an increase in the crystallite size up to 25 nm as compared to 10 nm for the **BTPT-4F-OD** sample. Indexation followed by Pawley refinement yielded similar monoclinic cells P2 symmetry with the following parameters: a = 31.4 Å, b = 5.1 Å, c = 24.0 Å, β = 87.5° for **BTPT-OD** and a = 26.7 Å, b = 4.99 Å, c = 25.1 Å, β = 87.3° for **BTPT-4F-OD**. The number of molecules per crystal cell equals 2 for both cases. The cell volumes and the angles are almost identical, and the low b value suggests that π-π stacking occurs along the 0k0 planes. Therefore, the molecules are located flatwise in the ac plane. This assumption was confirmed by the Reflex solve processed in the Biovia Material Studio software package. The model obtained by the parallel tempting balancing the R_{wp}

value of the simulated diffraction pattern and the V_dW close contacts energy is presented in Figure 3c.

3.4. Photovoltaic Properties

To obtain a clearer understanding of the difference in photovoltaic performance between **BTPT-4F-OD** and **BTPT-OD** non-fullerene acceptors, we blended them with a PM6 donor to prepare a bulk heterojunction (BHJ) photovoltaic active layer system. The overall device structure adopts the traditional forward structure of glass/indium tin oxide (ITO)/poly(3,4-ethylenedioxythiophene): poly(styrenesulfonate)(PEDOT:PSS)/PM6:BTPT-4F-OD or PM6:BTPT-OD/PNDIT-F3N/Ag (Figure 4a).

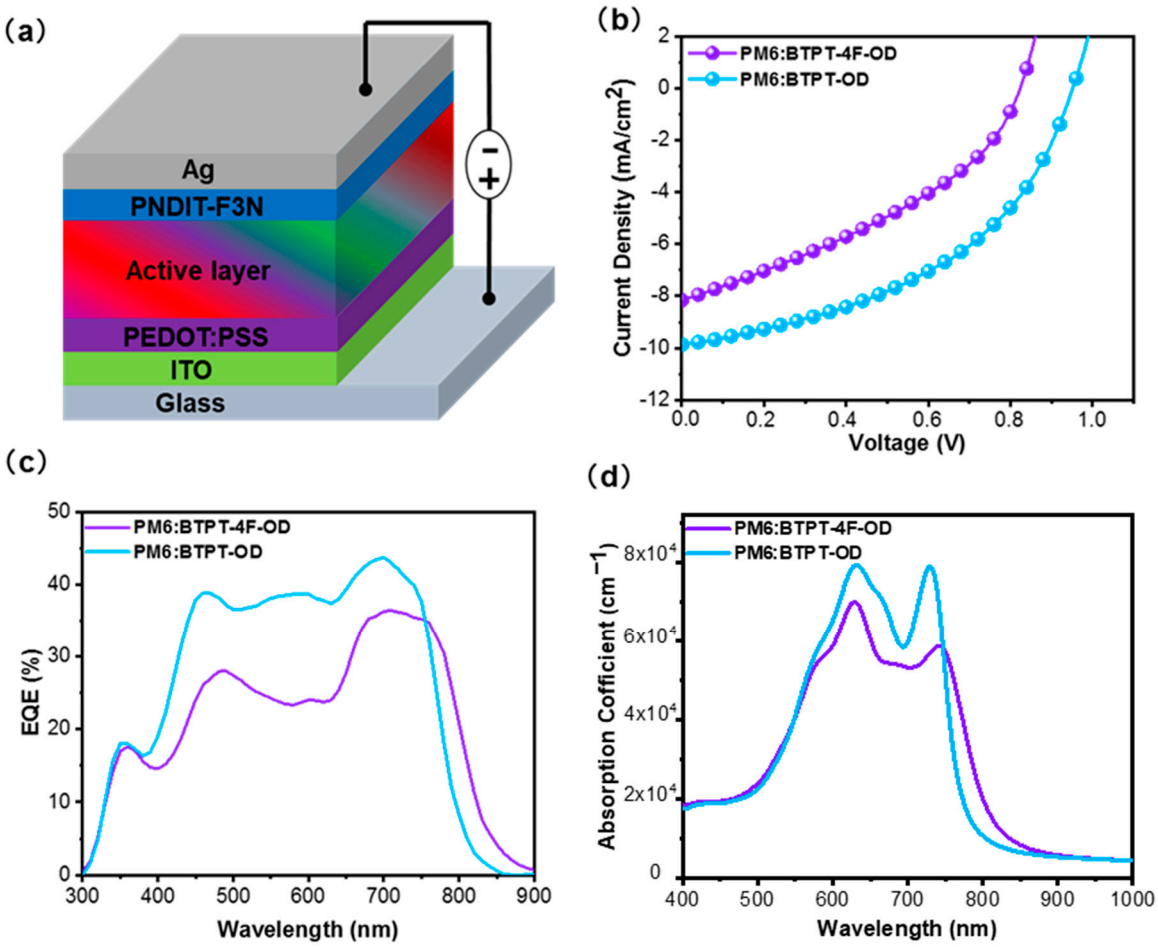

Figure 4. (**a**) Schematic device structure; (**b**) *J-V* characteristics for devices based on PM6: BTPT-4F-OD and PM6: BTPT-OD blends; (**c**) Corresponding EQE spectra of PM6: BTPT-4F-OD and PM6: BTPT-OD-based devices; (**d**) Absorption coefficient spectra of PM6: BTPT-4F-OD and PM6: BTPT-OD films.

The optimized devices based on PM6:BTPT-4F-OD and PM6:BTPT-OD were obtained under similar processing conditions, which were provided in Table 2. The relevant current density-voltage (*J-V*) characteristics of the corresponding devices are shown in Figure 4b. The devices based on PM6:BTPT-4F-OD showed a V_{OC} of 0.824 V, a J_{SC} of 8.16 mA/cm^2, and a FF of 36.9%, delivering a PCE of 2.48%. The PM6:BTPT-OD devices exhibited an elevated PCE of 4.30% with a high V_{OC} of 0.952 V, an increased J_{SC} of 9.86 mA/cm^2, and a FF of 43.3%. The corresponding external quantum response efficiency is shown in Figure 4c. It can be seen that the PM6:BTPT-OD system has a stronger response degree between 350 and 750 nm in the visible region, and the highest external quantum efficiency (EQE) value is close to 45%, while the PM6:BTPT-4F-OD system response range is concentrated between

350 and 800 nm, with a wider EQE response, but its level is much weaker than that of the BTPT-OD system, with a maximum value of only 36%. By analyzing the absorption spectra of PM6, BTPT-4F-OD, and BTPT-OD, it can be found that the maximum absorption peak of **BTPT-4F-OD** is at 762 nm, with a shoulder at 692 nm. However, **BTPT-OD** has bluer absorption with the shoulders at 673 nm and the absorption maxima at 734 nm. In addition, it was found that the PM6:BTPT-OD system had a higher light absorption intensity by testing the absorption coefficient of the binary films (Figure 4d). All these results indicate that **BTPT-OD** had better photovoltaic performance, which could also explain the higher J_{SC} and PCE of the PM6:BTPT-OD system.

Table 2. Specific device performance of the binary devices under the processing condition of AM 1.5G (100 mW/cm^2).

Active Layer	V_{OC} (V)	J_{SC} (J_{calc}) [a] (mA/cm^2)	FF (%)	PCE (%, PCE_{avg} [b])
PM6:BTPT-4F-OD	0.824	8.16 (7.84)	36.9	2.48 (2.32 ± 0.13)
PM6:BTPT-OD	0.952	9.86 (9.70)	43.3	4.30 (4.19 ± 0.12)

[a] The J_{calc} calculated from the EQE spectrum. [b] The average values with the standard deviation were obtained from 10 devices.

To elucidate the exciton dynamics and charge transfer dynamics in these active layers, photoluminescence (PL) quenching experiments were performed. The PL spectra of PM6 pure film, PM6:BTPT-4F-OD, and PM6:BTPT-OD blend films are depicted in Figure 5a. It can be seen that PM6 exhibits a strong fluorescence effect at the excitation wavelength of 532 nm. When blended with **BTPT-4F-OD**, the PL quenching efficiency of its excitons is 65.9%, while the system blended with **BTPT-OD** has an increased quenching efficiency of 79.3%. This indicates that the **BTPT-OD** system has better exciton use efficiency. In addition, we analyze the kinetic process of excitons from the maps of saturation current and effective bias. The saturation current is the difference between the photocurrent and the dark current. The effective bias voltage is equal to V_0 minus V_a. V_0 represents the voltage when the saturation current is 0, and V_a is the applied bias voltage. The exciton dissociation efficiency (η_{diss}) of the devices can be calculated by the J_{ph}/J_{sat} values under short-circuit conditions, PM6:BTPT-OD-based devices displayed much higher η_{diss} than PM6:BTPT-4F-OD-based devices (82.9% vs. 70.5%).

To monitor the charge transport ability of the system, the mobility of the system was measured using the space-charge-limited-current (SCLC) method. The electron mobility and hole mobility of PM6:BTPT-4F-OD is 3.52×10^{-4} and 1.94×10^{-4} cm^{2}V^{-1}s^{-1}, respectively, while that of the PM6:BTPT-OD system is 4.39×10^{-4} and 2.86×10^{-4} cm^{2}V^{-1}s^{-1}. It can be seen that the latter not only has greater charge mobility, but also possess more balanced transport mobility, which is beneficial to increase the J_{SC} of the device and achieving higher PCE (Table 3). To further clarify the extinct changes in the J_{SC} and FF, the charge recombination was de-fined by measurement of J_{SC} and VOC changes under various light intensities (P) from 100 to 5 mW cm^{-2}. The relationship between J_{SC} and Plight can be summarized as a power-law equation of $J_{SC} \propto P\alpha$, which is employed to analyze the bimolecular recombination in OSC devices. The variation of V_{OC} relative to light intensity is represented by the slope n of nkT/q (Figure 5d,e). Compared with the PM6:BTPT-4F-OD system, PM6:BTPT-OD has a higher α value (0.975 vs. 0.885) and a smaller n value (1.18 vs. 1.24), indicating that the BTPT-OD system has less bimolecular recombination and trap-assisted recombination. Additionally, as demonstrated in Figure 5f,g, transient photocurrent (TPC) and transient photovoltage (TPV) were determined to evaluate the charge extraction time (τ_1) and charge carrier lifetimes (τ_2) in the corresponding devices. It can be seen that the τ_1 and τ_2 of the **BTPT-OD** system are 0.29 us and 5.3 us, respectively, while the τ_1 and τ_2 of the **BTPT-4F-OD** system are only 0.97 us and 3.0 us, which indicates that the former has faster charge extraction time and longer carrier lifetime, supporting the significant enhancement of J_{SC} and FF.

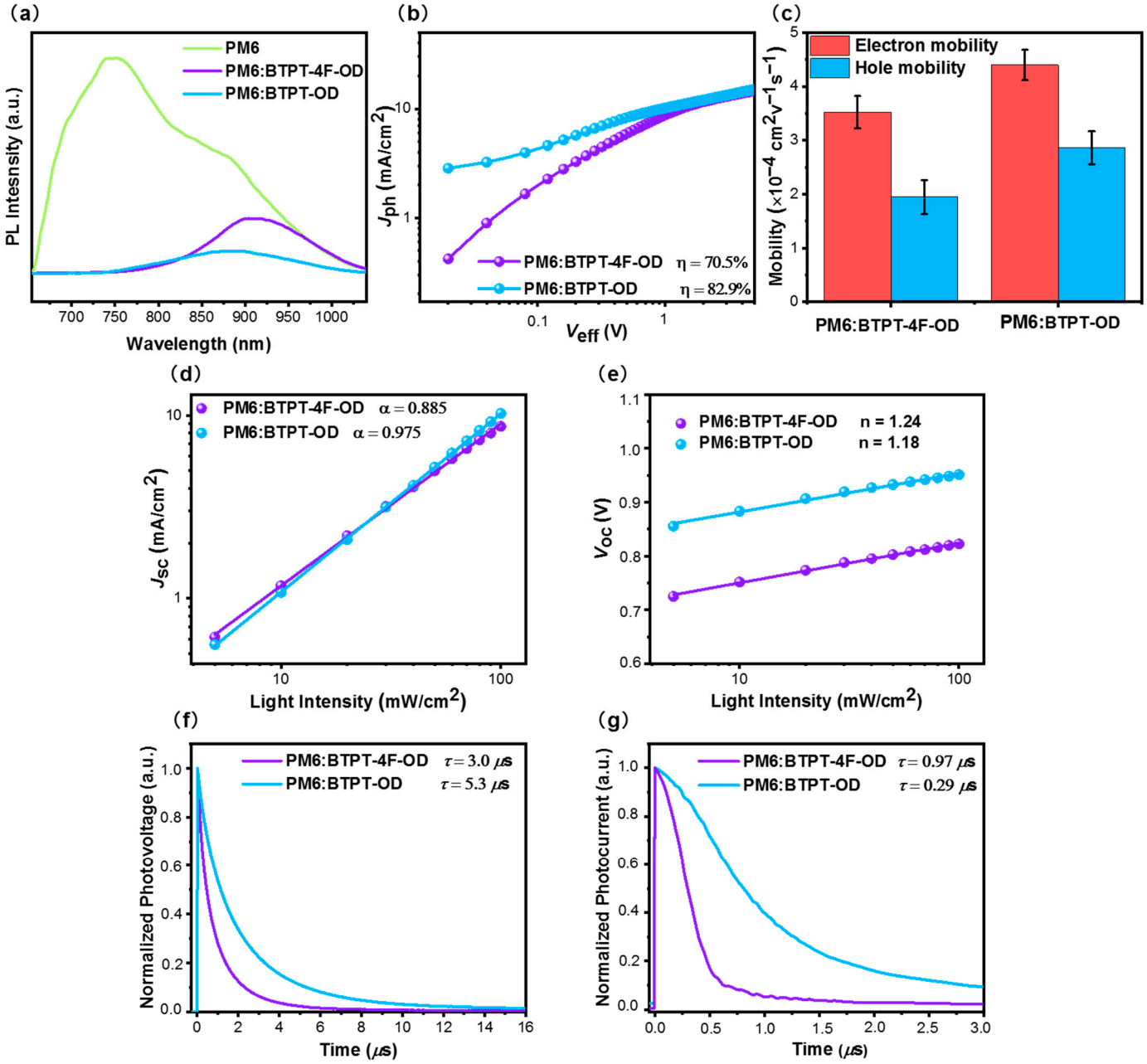

Figure 5. (**a**) Steady-state fluorescence patterns of PM6, PM6:BTPT-4F-OD, and PM6:BTPT-OD films; (**b**) J_{ph} versus V_{eff} curves; (**c**) electron and hole mobility; (**d**) J_{SC} versus P_{light}; (**e**) V_{OC} versus P_{light}; (**f**) transient photocurrent, and; (**g**) transient photovoltage plots of PM6:BTPT-4F-OD and PM6:BTPT-OD devices.

Table 3. Parameters of electron mobility and hole mobility of PM6:BTPT-4F-OD and PM6: BTPT-OD devices).

Device	μ_e (×10^{-4} cm^2 V^{-1} s^{-1})	μ_h (×10^{-4} cm^2 V^{-1} s^{-1})	μ_e/μ_h
PM6:BTPT-4F-OD	3.52 ± 0.25	1.94 ± 0.31	1.81
PM6:BTPT-OD	4.39 ± 0.27	2.86 ± 0.28	1.53

To monitor the surface morphology and crystallization properties of the active layer, AFM characterization was performed for both systems. Root mean square (RMS) values of 1.21 nm and 0.77 nm were obtained for the PM6:BTPT-4F-OD (Figure 6a,b) and the PM6:BTPT-OD (Figure 6c,d) systems, respectively. The observed differences in sample

roughness suggested that the PM6:BTPT-OD system might have a more suitable distribution of donor and acceptor phases, facilitating a better interpenetrating network structure and, consequently, an adequate dissociation and efficient transport of excitons. Perhaps the improved microscopic morphology of the PM6:BTPT-OD system led to a higher PCE.

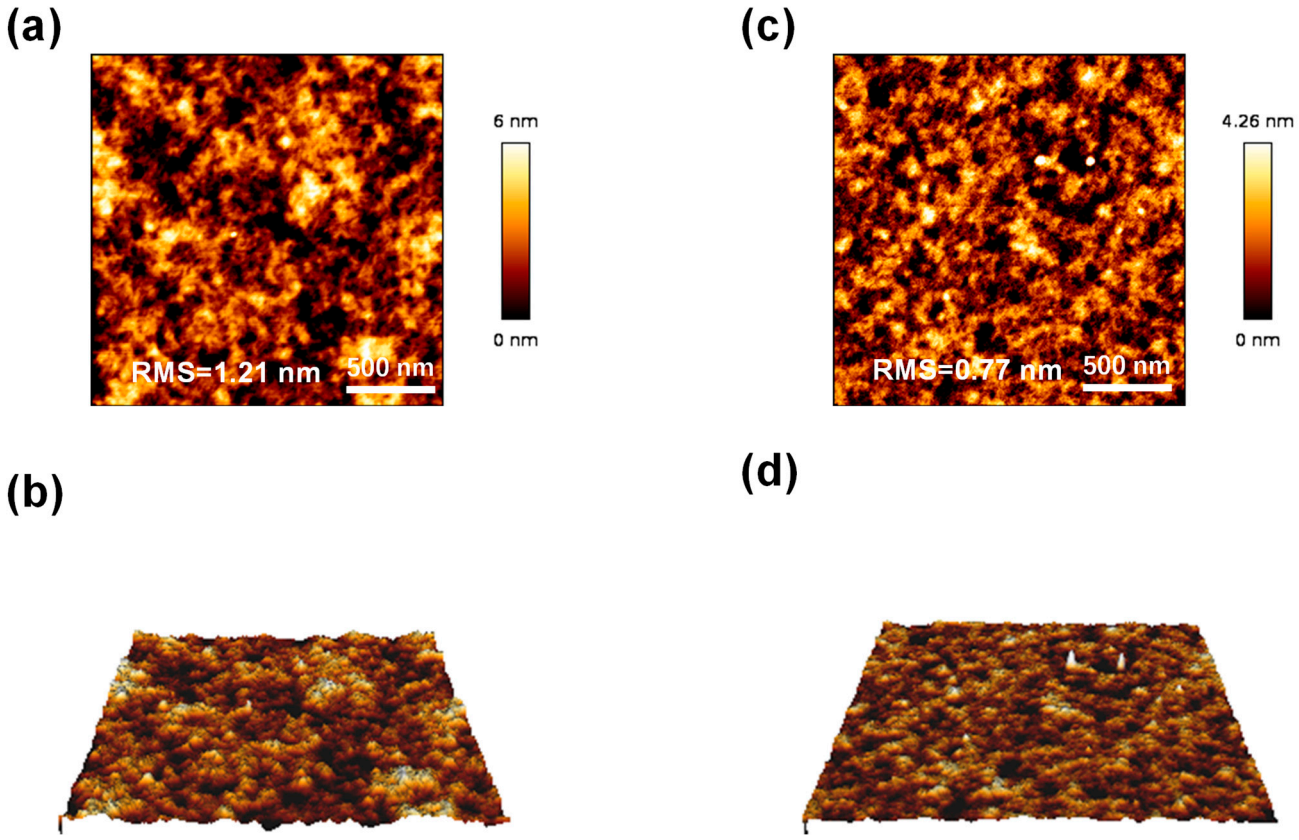

Figure 6. The AFM and relevant 3D images of: (**a**,**b**) PM6: BTPT-4F-OD and (**c**,**d**) PM6: BTPT-OD.

4. Conclusions

In conclusion, we successfully synthesized two novel non-fullerene acceptors **BTPT-OD** and **BTPT-4F-OD** with the simplest fused structures among Y-like NFAs. The acceptor molecules obtained have efficient light absorption in the visible and near-IR spectral range (700–950 nm), low LUMO energy levels (below −3.80 eV), high thermal stability (above 300 °C), as well as the absence of phase transitions in the device operating temperature range. The higher degree of photoresponsiveness, better charge dynamics performance, more rational exciton transport paths, and more balanced charge transport characteristics are the reasons why PM6:BTPT-OD exhibits better photovoltaic performance than PM6:BTPT-4F-OD. Despite the moderate PCEs obtained for OSCs based on novel NFAs, our work demonstrates that the choice of terminal acceptor group is of high importance for the molecular design of Y-like NFAs. Although a higher performance in OSCs was expected for the **BTPT-4F-OD** with 5,6-difluorindan-1-one-3-dicyanvinyl terminal acceptor group due to the red-shifted light absorption and lower LUMO energy, it exhibited almost two times lower PCE in devices as compared to its counterpart **BTPT-OD** with a much simpler acceptor group. We believe that further molecular design of the similar simple NFAs taking into account not only the type of terminal acceptor group but also side alkyl chain engineering will boost the performance of the OSCs.

Supplementary Materials: The following supporting information can be downloaded at: https://www.mdpi.com/article/10.3390/en16083443/s1, Supplementary Information (NMR, and OSCs data) to this article can be found online.

Author Contributions: Conceptualization and Methodology, Y.N.L., J.M. and S.A.P.; Investigation, A.V.B. and J.W.; Resources and Investigation, E.D.P., D.O.B. and I.V.D.; Writing—Original Draft Preparation, E.D.P. and J.W.; Writing—Review and Editing, Y.N.L., E.D.P., J.W., J.M., A.V.B. and S.A.P.; Supervision, Y.N.L. and J.M.; Project Administration, J.M. and S.A.P. All authors have read and agreed to the published version of the manuscript.

Funding: The work on the synthesis and characterization of BTPT-OD and BTPT-4F-OD was financially supported by the Russian Science Foundation (21-43-00051). The work on OSCs was financially supported by the National Natural Science Foundation of China (NSFC) (Grant No. 52061135206). The NMR spectra were recorded using the equipment of the Collaborative Access Center "Center for Polymer Research" of Enikolopov Institute of Synthetic Polymeric Materials of the Russian Academy of Sciences under financial support from the Ministry of Science and Higher Education of the Russian Federation (topic FFSM-2021-0005).

Data Availability Statement: Data are included within the manuscript.

Acknowledgments: The authors acknowledge O.A. Maloshitskaya for recording MALDI-TOF spectra, S.M. Peregudova for CV experiments, and N.M. Surin for the recording of absorption spectra.

Conflicts of Interest: The authors declare no conflict of interest.

References

1. Zhang, G.; Zhao, J.; Chow, P.C.Y.; Jiang, K.; Zhang, J.; Zhu, Z.; Yan, H.; Huang, F.; Yan, H. Non-fullerene Acceptor Molecules for Bulk Heterojunction Organic Solar Cells. *Chem. Rev.* **2018**, *118*, 3447–3507. [CrossRef] [PubMed]
2. Riede, M.; Spoltore, D.; Leo, K. Organic Solar Cells—The Path to Commercial Success. *Adv. Energy Mater.* **2021**, *11*, 2002653. [CrossRef]
3. Mahmood, A.; Wang, J.L. Machine Learning for High Performance Organic Solar Cells: Current Scenario and Future Prospects. *Energy Environ. Sci.* **2021**, *14*, 90–105. [CrossRef]
4. Moser, M.; Wadsworth, A.; Gasparini, N.; McCulloch, I. Challenges to the Success of Commercial Organic Photovoltaic Products. *Adv. Energy Mater.* **2021**, *11*, 2100056. [CrossRef]
5. Kini, G.P.; Jeon, S.J.; Moon, D.K. Latest Progress on Photoabsorbent Materials for Multifunctional Semitransparent Organic Solar Cells. *Adv. Funct. Mater.* **2021**, *31*, 2007931. [CrossRef]
6. Sun, R.; Wu, Y.; Yang, X.; Gao, Y.; Chen, Z.; Li, K.; Qiao, J.; Wang, T.; Guo, J.; Liu, C.; et al. Single-Junction Organic Solar Cells with 19.17% Efficiency Enabled by Introducing One Asymmetric Guest Acceptor. *Adv. Mater.* **2022**, *34*, 2110147. [CrossRef] [PubMed]
7. Cui, Y.; Xu, Y.; Yao, H.; Bi, P.; Hong, L.; Zhang, J.; Zu, Y.; Zhang, T.; Qin, J.; Ren, J.; et al. Single-Junction Organic Photovoltaic Cell with 19% Efficiency. *Adv. Mater.* **2021**, *33*, 2102420. [CrossRef] [PubMed]
8. Bi, P.; Zhang, S.; Chen, Z.; Xu, Y.; Cui, Y.; Zhang, T.; Ren, J.; Qin, J.; Hong, L.; Hao, X.; et al. Reduced Non-Radiative Charge Recombination Enables Organic Photovoltaic Cell Approaching 19% Efficiency. *Joule* **2021**, *5*, 2408–2419. [CrossRef]
9. Zhu, L.; Zhang, M.; Xu, J.; Li, C.; Yan, J.; Zhou, G.; Zhong, W.; Hao, T.; Song, J.; Xue, X.; et al. Single-Junction Organic Solar Cells with over 19% Efficiency Enabled by a Refined Double-Fibril Network Morphology. *Nat. Mater.* **2022**, *21*, 656–663. [CrossRef]
10. Chiristina, E.N.; Rahayu, S.U.; Tubtimtae, A.; Shi, J.-B.; Lee, M.-W. Rare-Earth-Incorporated Ternary Ce x Cd 1−x S Quantum Dot-Sensitized Solar Cells. *RSC Adv.* **2022**, *12*, 31093–31101. [CrossRef]
11. Sun, S.; Xu, M.; Zhang, Y.; Liu, R.; Wang, X.; Zhang, L.; Fang, Y.; Wang, P. Study of Molybdenum Oxide Optimized Hole Carrier Transport in Perovskite Solar Cells. *Org. Electron.* **2023**, *113*, 106697. [CrossRef]
12. Tai, Q.; Yan, F. Emerging Semitransparent Solar Cells: Materials and Device Design. *Adv. Mater.* **2017**, *29*, 1700192. [CrossRef] [PubMed]
13. Guo, F.; Ameri, T.; Forberich, K.; Brabec, C.J. Semitransparent Polymer Solar Cells. *Polym. Int.* **2013**, *62*, 1408–1412. [CrossRef]
14. Dai, S.; Zhan, X. Nonfullerene Acceptors for Semitransparent Organic Solar Cells. *Adv. Energy Mater.* **2018**, *8*, 1800002. [CrossRef]
15. Li, Y.; Xu, G.; Cui, C.; Li, Y. Flexible and Semitransparent Organic Solar Cells. *Adv. Energy Mater.* **2018**, *8*, 1701791. [CrossRef]
16. Landerer, D.; Bahro, D.; Röhm, H.; Koppitz, M.; Mertens, A.; Manger, F.; Denk, F.; Heidinger, M.; Windmann, T.; Colsmann, A. Solar Glasses: A Case Study on Semitransparent Organic Solar Cells for Self-Powered, Smart, Wearable Devices. *Energy Technol.* **2017**, *5*, 1936–1945. [CrossRef]
17. Hollingsworth, J.A.; Ravishankar, E.; O'Connor, B.; Johnson, J.X.; DeCarolis, J.F. Environmental and Economic Impacts of Solar-Powered Integrated Greenhouses. *J. Ind. Ecol.* **2020**, *24*, 234–247. [CrossRef]
18. Sumaiya, S.; Kardel, K.; El-Shahat, A. Organic Solar Cell by Inkjet Printing—An Overview. *Technologies* **2017**, *5*, 53. [CrossRef]
19. Xue, P.; Cheng, P.; Han, R.P.S.; Zhan, X. Printing Fabrication of Large-Area Non-Fullerene Organic Solar Cells. *Mater. Horizons* **2022**, *9*, 194–219. [CrossRef]
20. Burlingame, Q.; Huang, X.; Liu, X.; Jeong, C.; Coburn, C.; Forrest, S.R. Intrinsically Stable Organic Solar Cells under High-Intensity Illumination. *Nature* **2019**, *573*, 394–397. [CrossRef]
21. Leonard, N.G.; Lee, S.W.; Chang, D.W.; Hodgkiss, J.M.; Vak, D. Organic Photovoltaics' New Renaissance: Advances Toward Roll-to-Roll Manufacturing of Non-Fullerene Acceptor Organic Photovoltaics. *Adv. Mater. Technol.* **2022**, *7*, 2101556. [CrossRef]

22. Peng, C.; Huang, Y.; Wu, Z. Building-integrated photovoltaics (BIPV) in architectural design in China. *Energy Build.* **2011**, *43*, 3592–3598. [CrossRef]
23. Biyik, E.; Araz, M.; Hepbasli, A.; Shahrestani, M.; Yao, R.; Shao, L.; Essah, E.; Oliveira, A.C.; del Caño, T.; Rico, E.; et al. A Key Review of Building Integrated Photovoltaic (BIPV) Systems. *Eng. Sci. Technol. Int. J.* **2017**, *20*, 833–858. [CrossRef]
24. Fan, B.; Zhang, D.; Li, M.; Zhong, W.; Zeng, Z.; Ying, L.; Huang, F.; Cao, Y. Achieving over 16% efficiency for single-junction organic solar cells. *Sci. China Chem.* **2019**, *62*, 746–752. [CrossRef]
25. Zhao, J.J.; Yao, C.; Ali, M.U.; Miao, J.; Meng, H. Recent Advances in High-performance Organic Solar Cells Enabled by Acceptor-Donor-Acceptor-Donor-Acceptor (A-DA′D-A) Type Acceptors. *Mater. Chem. Front.* **2020**, *4*, 3487–3504. [CrossRef]
26. Yuan, J.; Zhang, Y.; Zhou, L.; Zhang, G.; Yip, H.-L.; Lau, T.-K.; Zou, Y.; Zhu, C.; Peng, H.; Johnson, P.A.; et al. Single-Junction Organic Solar Cell with over 15% Efficiency Using Fused-Ring Acceptor with Electron-Deficient Core. *Joule* **2019**, *3*, 1140–1151. [CrossRef]
27. Luo, D.; Jang, W.; Babu, D.D.; Kim, M.S.; Wang, D.H.; Kyaw, A.K.K. Recent progress in organic solar cells based on non-fullerene acceptors: Materials to devices. *J. Mater. Chem. A* **2022**, *10*, 3255–3295. [CrossRef]
28. He, Q.; Ufimkin, P.; Aniés, F.; Hu, X.; Kafourou, P.; Rimmele, M.; Rapley, C.L.; Ding, B. Molecular engineering of Y-series acceptors for nonfullerene organic solar cells. *SusMat* **2022**, *2*, 591–606. [CrossRef]
29. Zhang, J.; Xiang, Y.; Zheng, S. From Y6 to BTPT-4F: A theoretical insight into the influence of the individual change of fused-ring skeleton length or side alkyl chains on molecular arrangements and electron mobility. *New J. Chem.* **2021**, *45*, 12247–12259. [CrossRef]
30. Ming, R.; Gao, J.; Gao, W.; Ning, W.; Luo, Z.; Zhang, F.; Yang, C. Benzo[c][1,2,5]thiadiazole-Fused Pentacyclic Small Molecule Acceptors for Organic Solar Cells. *Dyes Pigm.* **2020**, *185*, 108970. [CrossRef]
31. Qiu, W.; Zheng, S. Designing and Screening High-Performance Non-Fullerene Acceptors: A Theoretical Exploration of Modified Y6. *Sol. Rrl* **2022**, *5*, 2100023. [CrossRef]
32. Murugan, P.; Hu, T.; Hu, X.; Chen, Y. Fused ring A–DA′D–A (Y-series) non-fullerene acceptors: Recent developments and design strategies for organic photovoltaics. *J. Mater. Chem. A* **2022**, *10*, 17968–17987. [CrossRef]
33. Wang, J.; Xue, P.; Jiang, Y.; Huo, Y.; Zhan, X. The principles, design and applications of fused-ring electron acceptors. *Nat. Rev. Chem.* **2022**, *6*, 614–634. [CrossRef]
34. Uno, T.; Takagi, K.; Tomoeda, M. Synthesis of Bisfurazanobenzo-2, 1, 3-thiadiazole and Related Compounds. *Chem. Pharm. Bull.* **1980**, *28*, 909–1912. [CrossRef]
35. Pu, S.; Zheng, C.; Sun, Q.; Liua, G.; Fan, C. Enhancement of cyclization quantum yields of perfluorodiarylethenes via weak intramolecular interactions. *Chem. Commun.* **2013**, *48*, 8036–8038. [CrossRef]
36. Uddin, M.A.; Lee, T.H.; Xu, S.; Park, S.Y.; Kim, T.; Song, S.; Nguyen, T.L.; Ko, S.J.; Hwang, S.; Kim, J.Y.; et al. Interplay of Intramolecular Noncovalent Coulomb Interactions for Semicrystalline Photovoltaic Polymers. *Chem. Mater.* **2015**, *27*, 5997–6007. [CrossRef]
37. Yao, H.; Cui, Y.; Yu, R.; Gao, B.; Zhang, H.; Hou, J. Design, Synthesis, and Photovoltaic Characterization of a Small Molecular Acceptor with an Ultra-Narrow Band Gap Angew. *Chem. Int. Ed.* **2017**, *56*, 3045–3049. [CrossRef]
38. Ponomarenko, S.A.; Rasulova, N.N.; Luponosov, Y.N.; Surin, N.M.; Buzin, M.I.; Leshchiner, I.; Peregudova, S.M.; Muzafarov, A.M. Bithiophenesilane-Based Dendronized Polymers: Facile Synthesis and Properties of Novel Highly Branched Organosilicon Macromolecular Structures. *Macromolecules* **2012**, *45*, 2014–2024. [CrossRef]
39. Cardona, C.M.; Li, W.; Kaifer, A.E.; Stockdale, D.; Bazan, G.C. Electrochemical Considerations for Determining Absolute Frontier Orbital Energy Levels of Conjugated Polymers for Solar Cell Applications. *Adv. Mater.* **2011**, *23*, 2367–2371. [CrossRef]
40. Roncali, J.; Leriche, P.; Cravino, A. From one- to three-dimensional organic semiconductors: In search of the organic silicon? *Adv. Mater.* **2007**, *19*, 2045–2060. [CrossRef]
41. Kozlov, O.V.; Luponosov, Y.N.; Ponomarenko, S.A.; Kausch-Busies, N.; Paraschuk, D.Y.; Olivier, Y.; Beljonne, D.; Cornil, J.; Pshenichnikov, M.S. Ultrafast charge generation pathways in photovoltaic blends based on novel star-shaped conjugated molecules. *Adv. Energy Mater.* **2014**, *5*, 1401657. [CrossRef]
42. Roncali, J.; Grosu, I. The dawn of single material organic solar cells. *Adv. Sci.* **2019**, *6*, 1801026. [CrossRef] [PubMed]